Front. Chem. Sci. Eng. 2025, 19(12): 120
https://doi.org/10.1007/s11705-026-2635-9

RESEARCH ARTICLE

Co-reaction of methanol and alkanes with different carbon numbers over microsphere catalysts

Mingwei Peng[1], **Lei Shi** (✉)[1], **Jinzhe Li** (✉)[2], **Zhongmin Liu** (✉)[2]

1 School of Chemical Engineering, Shenyang University of Chemical Technology, Shenyang 110142, China
2 National Engineering Research Center of Lower-Carbon Catalysis Technology, Dalian National Laboratory for Clean Energy, Dalian Institute of Chemical Physics, Chinese Academy of Sciences, Dalian 116023, China

Abstract The co-reaction of methanol with C_5–C_{16} *n*-alkanes was investigated over microsphere catalysts with varying surface acidity and ZSM-5 as the active components. The results indicate that, as the carbon number of alkanes increases, the formation of C_1–C_4 alkanes decreases while the production of C_2–C_4 alkenes increases on the catalyst with weak outer surface acidity. This suggests that side reactions such as alkene aromatization and hydrogen transfer are suppressed. Conversely, on the catalyst with strong outer surface acidity, further reaction of olefins significantly increases, leading to a gradual decrease in light olefin yield and a corresponding increase in benzene, toluene, xylene, and heavy aromatics. Additionally, it is observed that long-chain *n*-alkanes (the kinetic diameter of *n*-hexadecane exceeds the pore size of ZSM-5 zeolite, the active component in the microspherical catalyst) cannot enter the internal pores of ZSM-5, resulting in primary cracking due to the acidic sites on the outer surface. However, long-chain *n*-alkanes can adjust their molecular orientation on pure ZSM-5 zeolites and enter the pore structure, leading to alkane cracking influenced by both internal and external surface acidity. These findings provide valuable guidance for the design of industrial catalysts, particularly in terms of pore size and acidity.

Keywords ZSM-5, methanol, *n*-hexadecane, C_5–C_{16} alkanes, olefin yield, coupling conversion

1 Introduction

Catalytic cracking has solidified its role as a cornerstone technology for light olefin production, particularly in the context of heavy oil processing, which serves as a vital industrial pathway for synthesizing propylene, butene, and environmentally friendly transportation fuels [1–4]. In recent years, methanol conversion and hydrocarbon cracking have emerged as key technologies in the petrochemical and energy sectors, achieving significant advancements in catalyst design process optimization. In China, representative technologies include the DMTO process developed by the Dalian Institute of Chemical Physics, Chinese Academy of Sciences. After improvements this process achieves 100% methanol conversion and 90% selectivity for light olefins (C_2–C_4) [5]. In catalyst development, various metals, such as manganese, calcium, potassium, strontium, lanthanum, gallium, and cerium-have been applied to modify ZSM-5 zeolites [6–9], enhancing the catalytic performance and stability of MTO catalysts. Xia et al. [10] prepared a strontium-modified ZSM-5 catalyst for naphtha catalytic cracking and found that the modification reduced the number of acid sites on the zeolite, inhibiting hydrogen transfer reactions while promoting dehydrogenation cracking.

Hydrocarbon cracking, inherently a highly endothermic process, stands in stark contrast to the methanol-to-olefins reaction [11–13], a thermodynamically exothermic, non-petroleum-based route to light olefins [14–17]. Both reactions occur on acidic zeolite catalysts, and their co-feeding can enable efficient energy utilization while allowing precise regulation of the product distribution to enhance selectivity toward high-value-added chemicals such as aromatics and light olefins. ZSM-5 molecular sieves, distinguished by their three-dimensional microporous architecture, shape-selective catalysis, and modifiable acid properties, remain the catalyst of choice for large-scale applications such as fluidized catalytic cracking [18–22]. Jung et al. [23] investigated the catalytic cracking of *n*-octane using several types of zeolite catalysts and demonstrated that ZSM-5 zeolite exhibits

Received September 28, 2025; accepted October 20, 2025;
online December 1, 2025

E-mails: shilei@syuct.edu.cn (Shi L.), lijinzhe@dicp.ac.cn (Li J.),
liuzm@dicp.ac.cn (Liu Z.)

high catalytic activity for light olefin production. Researchers have reported the influence of reactant carbon number (i.e., chain length) on branched hydrocarbon formation during the isomerization of linear alkanes catalyzed by metal-loaded zeolite catalysts [24]. Despite these insights, critical gaps persist in understanding the co-conversion of methanol with long-chain *n*-alkanes (C_{10+}), and the effect of carbon number of *n*-alkanes on the production of propylene and ethylene by catalytic cracking has not been reported. Addressing these challenges is pivotal for advancing integrated catalytic systems that maximize olefin yields while minimizing energy penalties and secondary reactions.

This study systematically investigates the co-conversion behaviors of *n*-alkanes with methanol over microspherical catalysts, with emphasis on elucidating the cracking reaction pathways of *n*-alkanes with varying carbon chain lengths. Furthermore, it clarifies the characteristics of the cracking of long-chain alkanes catalyzed by ZSM-5 zeolite. The fundamental principles established in this work provide crucial foundations for the rational design of high-efficient catalysts and processes in the coupling conversion applications.

2 Experimental

2.1 Catalyst preparation and reagents

ZSM-5 samples were obtained from the Nankai University Catalyst Factory. The microsphere catalysts with different surface acidity were prepared by combining ZSM-5 zeolites with different binders and calcined at 600 °C for 4 h. The samples were labeled as Cat.1$^{\#}$ and Cat.2$^{\#}$, and screened 80–120 mesh for reaction test. The catalysts after *n*-octane and *n*-hexadecane feed reactions were designated as Cat.1$^{\#}$-C_8, Cat.1$^{\#}$-C_{16}, Cat.2$^{\#}$-C_8, and Cat.2$^{\#}$-C_{16}, while Cat.1$^{\#}$-P and Cat.2$^{\#}$-P represent the pristine samples. The ZSM-5 zeolites after *n*-hexadecane feed reactions were designated as ZSM-5-C_{16}, while ZSM-5-P represents the pristine samples. Methanol (> 99.8%) and *n*-alkanes (> 98%) were purchased from the Bonuo Biochemical Reagent Factory in Dalian, China.

2.2 Characterization of catalysts and molecular sieves

The morphological characteristics of microsphere catalysts and molecular sieves were characterized by a Hitachi SU8020 scanning electron microscope (SEM) and a Hitachi TM3000 tabletop microscope.

The crystal structure and phase information of microsphere catalysts and ZSM-5 molecular sieve were analyzed by the X'Pert Pro X-ray diffractometer (XRD) of the PANalytical company. Specific test conditions: copper target, Kα ray (λ = 1.54187 nm), Ni filter, voltage 40 kV, tube current 40 mA, scanning range: 5°–60°, scanning speed: $5°\cdot min^{-1}$.

The surface area, pore volume, and pore structure of the samples were measured by an ASAP 2020 adsorption analyzer manufactured by Micromeritics, USA. The test procedure was as follows: 0.1 g of 40–60 mesh molecular sieve particles were weighed and loaded into the sample tube, and the samples were pretreated for 4 h at a temperature of 623 K under vacuum conditions to remove the water in the samples. Nitrogen physical adsorption and desorption experiments were carried out at a temperature of 77 K in liquid nitrogen. The specific surface area of the samples was obtained according to the Brunauer-Emmett-Teller formula, and the total pore volume was determined by the adsorption at a single point of pressure $P\cdot P_0^{-1} = 0.975$. The microporous area and pore volume of the samples were determined by the *t*-plot method.

The acid strength of the samples was analyzed by the Autochem II 2920 Chemisorption Analyzer manufactured by Micromeritics, USA, using ammonia as a probe. The test procedure was as follows: first, 0.15 g of the sample to be tested (particle size 40–60 mesh) was loaded into a U-shaped quartz tube, and the temperature was increased from room temperature to 623 K in a helium gas stream of $30\ mL\cdot min^{-1}$ before the test in order to remove the water in the sample. After cooling down to 423 K, ammonia was introduced until the sample was saturated with adsorption, and switched to helium purge to remove ammonia in the physically adsorbed state. Finally, the temperature was increased to 923 K using a ramp rate of $10\ K\cdot min^{-1}$, and the signal of ammonia concentration desorbed during the ramp was recorded in real time by a thermal conductivity detector.

The external surface acidity of the catalyst microspheres was analyzed using an XF808-4 infrared spectrometer with 2,6-di-*tert*-butylpyridine as the probe [25]. The process included: pressing 15 mg of sample powder into a 13 mm diameter pellet, dehydrating the pellet at 673 K under vacuum for 2 h, cooling to 423 K, introducing excess 2,6-di-*tert*-butylpyridine for 5 min, evacuating physically adsorbed probe molecules, desorbing at 423 K for 30 min, cooling to room temperature, and acquiring the result of Fourier transform infrared spectroscopy (FTIR). The difference spectrum between the adsorbed and original samples was used to analyze the surface acidity.

In situ diffuse reflectance infrared Fourier transform spectroscopy was obtained using a Bruker Tensor 27 infrared spectrometer equipped with an MCT detector. The spectral acquisition parameters were set as averaging 16 scans at a resolution of $4\ cm^{-1}$. The sample was first pretreated at 600 °C for 30 min, and then *n*-octane was introduced via a nitrogen carrier (N_2 flow rate: $20\ mL\cdot min^{-1}$, saturation tube temperature: 293.15 K). Finally, the infrared difference spectrum was obtained by subtracting the spectrum of the sample holder from the collected spectra.

First, 0.1 g of the recovered catalyst or molecular sieve was dissolved in 1 mL of 20% HF solution. Organic species were extracted with 1.5 mL of CH_2Cl_2, and the carbonaceous extract in the organic phase was subjected to mass spectral recording in positive ion mode on a Solarix XR 15-T FT-ICR mass spectrometer (Bruker Daltonics, Germany). The instrument was equipped with an Nd:YAG laser (λ = 335 nm), and the ionization laser signal frequency was set at 200 Hz.

The amount of carbon buildup in the catalyst after the reaction of alkanes was determined by a thermal analyzer model SDTQ600 from TA, USA. Specific test procedure: 15 mg catalyst sample was taken and increased from room temperature to 900 °C at a rate of 10 $°C \cdot min^{-1}$ in an air flow of 100 $mL \cdot min^{-1}$. The amount of carbon accumulation was determined by the calculation of Eq. (1):

$$X = (M_{100\,°C} - M_{900\,°C})/M_{100\,°C} \times 100\%, \qquad (1)$$

where X denotes the mass fraction of carbon deposited on the catalyst; $M_{100\ °C}$ and $M_{900\ °C}$ represent the catalyst mass at 100 °C and 900 °C, respectively.

2.3 Catalytic reaction

The catalytic reaction was conducted in a U-shaped quartz fluidized bed reactor. The catalyst was activated at 550 °C in a nitrogen (N_2) atmosphere for 30 min, and then cooled down to the desired reaction temperature. Once the required temperature stabilized, two microinjection pumps were employed to introduce various raw material components, which were transported to the catalyst bed via a carrier gas (N_2) with an initial flow rate of 100 $mL \cdot min^{-1}$. An Agilent GC 7890A gas chromatograph was utilized for automatic online sampling and analysis of the reaction product composition. The data were processed using the area normalization method. Analytical conditions included hydrogen flame ionization detector (FID), HP-FFAP (50 m × 0.320 mm) and PlotQ-HT (27.5 m × 0.53 mm × 20 μm) capillary columns, with the column oven temperature programmed from 60 to 220 °C.

3 Results and discussion

3.1 Crystal structure, acidity, and morphology of the samples

The SEM images of the catalyst microspheres and ZSM-5 zeolite employed in this study were given in the Fig. S1 (cf. Electronic Supplementary Material, ESM). The XRD patterns of the two catalysts as well as the two ZSM-5 molecular sieves are given in Fig. S2 (cf. ESM). The four samples showed obvious diffraction peaks representing the MFI structure at 7.9°, 8.9°, 23.1°, 23.3°, and 23.9°, with good crystallinity, which indicates that the two microsphere catalysts and the two ZSM-5 molecular sieves have similar crystal structures.

The acidity of the catalyst is the key factor affecting the reaction performance. The temperature programmed desorption of ammonia (NH_3-TPD) results of two catalysts with different acidity are given in Fig. S3(a) (cf. ESM), in which there are significant ammonia desorption signal peaks near 236 and 427 °C, which correspond to the weak and strong acid sites of the microsphere catalysts, respectively. There is a great degree of decrease in the weak acid sites and almost disappearance of the strong acid sites of Cat.$2^{\#}$ compared to the Cat.$1^{\#}$. This phenomenon is ascribed to the reduced Al-site density in the catalyst, leading to a gradual decline in both strong and weak acid concentrations, particularly exhibiting a more significant attenuation in weak acid site abundance. Due to the obvious acidity difference, it is hypothesized that it has a greater impact on the yield of the product and the feedstock conversion during the catalytic cracking process of the model compounds. Similarly, as given in Fig. S3(b) (cf. ESM) for ZSM-5 molecular sieves with different silica-aluminum ratios, ZSM-5(131) showed a different degree of decrease in the amount of acid in both weak and strong acidic sites compared to ZSM-5(50).

Brønsted (B) acid sites serve as the active centers for the catalytic cracking of alkanes [26,27]. To further elucidate the Brønsted acidity on the external surfaces of the two microsphere catalysts, 2,6-di-*tert*-butylpyridine, a probe molecule with a molecular size significantly larger than the pore diameter of microsphere catalyst, was employed for FTIR characterization. As shown in Fig. S4 (cf. ESM), a distinct vibrational peak near 1616 cm^{-1} was observed in the FTIR spectra, which corresponds to the interaction between 2,6-di-*tert*-butylpyridine and the acid sites. The intensity of this peak reflects the number of accessible surface acid sites capable of adsorbing the probe molecule, with higher intensity indicating stronger Brønsted acidity on the external surface. Based on the FTIR spectral analysis, the relative strength of surface Brønsted acidity between the two catalysts could be conclusively determined.

The detailed pore structure parameters of the two different outer surface acid catalysts are given in Table S1 and Fig. S5 (cf. ESM) from which the corresponding parameters of specific surface area, microporous surface area, outer surface area (except micropores), pore volume, microporous volume, and pore size distribution of the two fresh samples can be seen.

3.2 Effect of feedstock ratio on the co-feeding reaction performance of methanol and *n*-octane

Under reaction conditions of 500 °C, atmospheric pressure, *n*-octane/methanol carbon ratios of 100/0, 75/25, 50/50, 25/75, and 0/100 (for example, the *n*-octane/methanol ratio of 75/25 means that the carbon molar content of methanol in the feed is 25% and that of *n*-octane is 75%, and so the corresponding *n*-octane/methanol molar ratio is 3:8), weight hourly space velocity (WHSV) of 0.98 g·g^{-1}·h^{-1}, and a time-on-stream of 5.5 min, the effect of feedstock ratio on the co-feeding reaction performance of methanol and *n*-octane over Cat.1$^{\#}$ was investigated. As shown in Fig. 1, methanol was completely converted throughout the process, and the conversion of *n*-octane gradually increased with the increasing methanol content in the feed, indicating that methanol promotes the activation of *n*-octane. Meanwhile, due to the autocatalytic properties of methanol, the presence of *n*-octane also accelerates methanol conversion, reflecting the synergistic effect between the two reactants. In the single *n*-octane cracking reaction, the dominant mechanism is monomolecular cracking, yielding mainly low-carbon hydrocarbons (C_2–C_4). Upon methanol addition, the cracking of *n*-octane shifts to a bimolecular mechanism, with isobutane as a typical product. During the reaction, intermediate olefins are prone to deep reactions to form higher hydrocarbons, which can either crack into light olefins or be converted into aromatics and alkanes. As the methanol content increases, the yields of benzene and toluene in the aromatic products gradually decrease, while those of xylene and C_{9+} aromatics increase. This is likely due to the strong methylation ability of methanol, which can directly react with benzene and toluene to form xylene and polymethylbenzenes.

3.3 Reaction patterns of co-feeding *n*-alkanes with methanol over microsphere catalysts

The reaction behavior of co-feeding C_5–C_{16} *n*-alkanes with methanol over Cat.1$^{\#}$ and Cat.2$^{\#}$ was investigated under the following conditions: a mass ratio of alkane to methanol of 9, a reaction temperature of 600 °C, atmospheric pressure, a total WHSV of 1 g·g^{-1}·h^{-1}, and a nitrogen carrier gas flow rate of 100 mL·min^{-1}. As shown in Figs. 2(a) and 2(c), the conversion of *n*-alkanes over both microsphere catalysts increased with higher carbon numbers, consistent with previous studies on *n*-alkane isomerization [28]. In this experiment, the dominance of the bimolecular cracking mechanism was driven by the combined effects of a relatively high proportion of alkanes, a relatively low feed space velocity, and the synergistic action of methanol. Meanwhile, monomolecular cracking also plays a secondary role: the light components (H_2O) generated from methanol decomposition may locally dilute the alkane concentration [29], slightly inhibiting the bimolecular pathway. Additionally, a small fraction of short-chain alkanes (e.g., *n*-pentane and *n*-hexane) may undergo direct monomolecular cracking to produce C_1–C_2 products (methane and ethylene), particularly near the strong acid sites of the catalyst.

As illustrated in Figs. 2(a) and 2(b), over the Cat.1$^{\#}$ with strong acidity and high acid density, the yields of C_1–C_4 alkanes progressively diminish with increasing carbon number of *n*-alkanes. This trend is attributed to the enhanced propensity of olefinic products to undergo secondary reactions, including cracking, disproportionation, oligomerization, and hydrogen transfer. Significantly, ethylene can be generated not only from the primary cracking of alkanes but also via secondary reactions of C_3–C_4 olefins. Consequently, the ethylene yield increases progressively throughout the reaction and remains significantly higher than that of propylene. Moreover, the ethylene and propylene yield rise further with increasing carbon numbers of *n*-alkanes. Longer *n*-alkanes substantially enhance the likelihood of secondary reactions occurring on the strong acid sites of the catalyst, leading to increased yields of BTX (benzene, toluene, xylene) and C_{9+} hydrocarbons, as well as accelerated carbon deposition. To better elucidate the cracking patterns of the feed system, the Cat.2$^{\#}$ with weaker surface acidity was selected for comparison. As shown in Table S1 (cf. ESM), Cat.1$^{\#}$ and Cat.2$^{\#}$ demonstrate comparable micropore volumes, while Cat.2$^{\#}$ exhibits a significantly higher

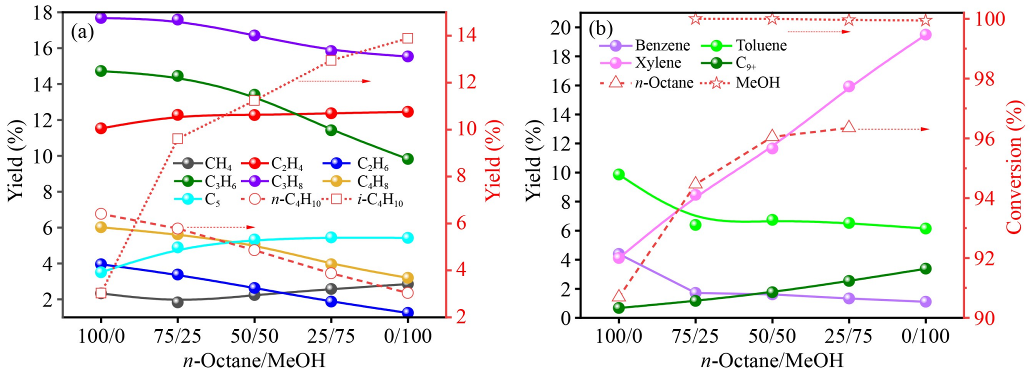

Fig. 1 Effect of feedstock ratio on the co-feeding reaction performance of methanol and *n*-octane. (a) C_1–C_5 product yields and (b) reactant conversion and benzene, toluene, and xylene (BTX) yields. Reaction conditions: T = 500 °C, atmospheric pressure, $\mathrm{WHSV}_{\mathrm{CH_2}}$ = 0.98 g·g^{-1}·h^{-1}, the total number of carbon atoms in the system is held constant, water content in methanol balanced by reducing the flow rate of carrier gas (N_2), reaction time = 5.5 min.

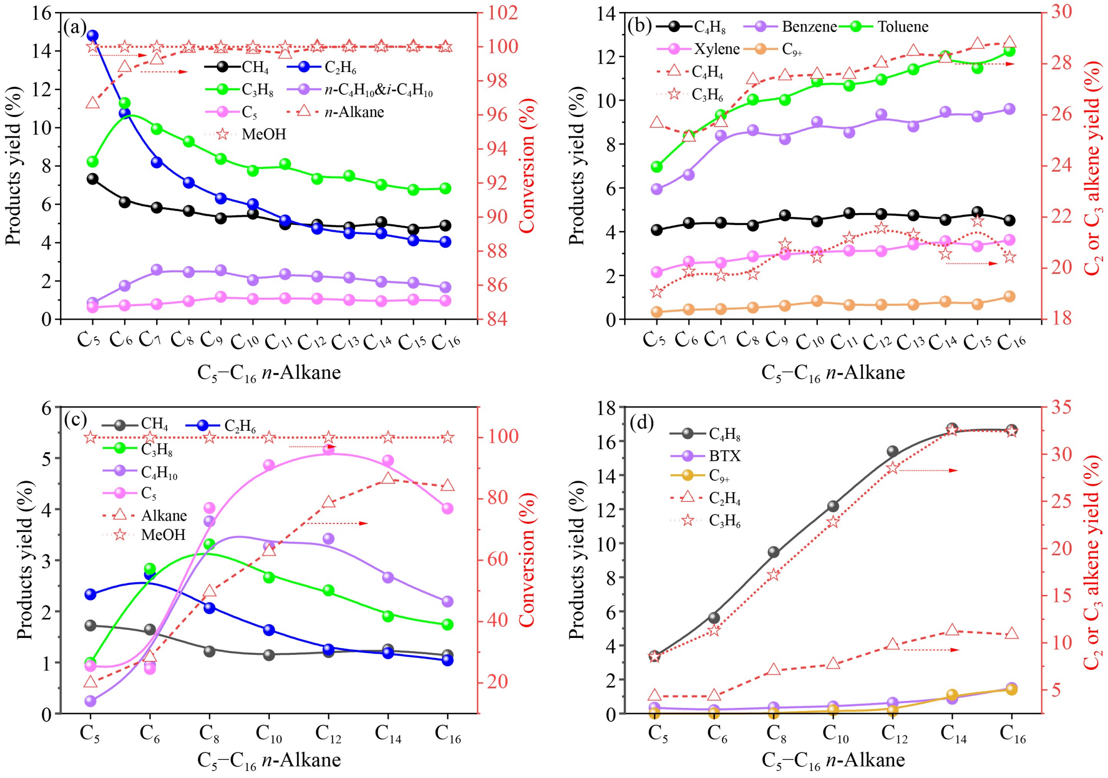

Fig. 2 The conversion and product yields of co-feeding *n*-alkanes and methanol. Changes in reactant conversion and product yield of (a, b) Cat.1# and (c, d) Cat.2#. Reaction conditions: T = 600 °C, atmospheric pressure, alkane WHSV = 0.9 $g \cdot g^{-1} \cdot h^{-1}$, methanol WHSV = 0.1 $g \cdot g^{-1} \cdot h^{-1}$, carrier gas ($N_2$) flow rate of 100 $mL \cdot min^{-1}$, TOS = 5.5 min.

total pore volume than Cat.1#. Previous studies have demonstrated that introducing mesoporous or macroporous structures can regulate the mass transfer capability of catalysts [30–32]. As illustrated in Fig. 2(c) and 2(d), the probability of secondary reactions such as oligomerization and cyclization of olefin products is significantly reduced on Cat.2#. Notably, the yields of BTX and C_{9+} hydrocarbons are extremely low for *n*-alkanes of varying carbon numbers, while the yields of C_1–C_3 alkanes are relatively small. Instead, the yields of C_4–C_5 hydrocarbons are higher, and the products are dominated by C_2–C_4 olefins. Unlike the behavior observed on Cat.1#, propylene is less prone to secondary cracking over weakly acidic catalysts, and its yield surpasses that of ethylene as the carbon number of alkanes increases. In summary, higher acid density promotes alkane cracking and ethylene formation but inhibits propylene production, whereas moderate acid density favors enhanced propylene yield.

3.4 Cracking of long-chain alkanes over ZSM-5 zeolite

ZSM-5 zeolite is characterized by a distinctive framework comprising two intersecting 10-membered ring channel systems, with pore apertures of 0.51 nm × 0.55 nm (straight channels) and 0.53 nm × 0.56 nm (sinusoidal channels), respectively [33]. However, the minimum-energy conformation of *n*-hexadecane (*n*-C_{16}) exhibits cross-sectional dimensions of 0.621 nm × 0.699 nm [34], exceeding the nominal pore size of ZSM-5. To systematically explore the structure-activity relationship, *n*-hexadecane was selected as a model compound for investigating the catalytic cracking behavior of long-chain *n*-alkanes over ZSM-5 zeolite. According to Fig. S3(b) (cf. ESM), the ZSM-5(131) zeolite exhibits significantly weaker acidity compared to ZSM-5(50). As shown in Figs. 3(a) and 3(d), the insufficient acidity of ZSM-5(131) fails to provide high catalytic activity, leading to a rapid decline in *n*-hexadecane conversion with prolonged reaction time. In contrast, ZSM-5(50) zeolite possesses higher acidity, resulting in superior catalytic performance and slower deactivation rates. Previous studies have indicated that the deactivation mechanism of ZSM-5 zeolites during alkane cracking is primarily attributed to coke deposition on the external surface [35–43]. Table S2 (cf. ESM) reveals the pore structures of ZSM-5 zeolites with different silicon-aluminum ratios before and after the reaction.

Molecular dynamics simulations demonstrate that alkanes undergo dynamic conformational adjustments at elevated temperatures, such as partial chain folding or torsional distortion, thereby reducing their effective cross-sectional area to enter pores. These findings align with experimental observations in industrial diesel dewaxing processes, where *n*-alkanes larger than *n*-C_{16} have been reported to access ZSM-5 channels through thermally activated conformational adaptations.

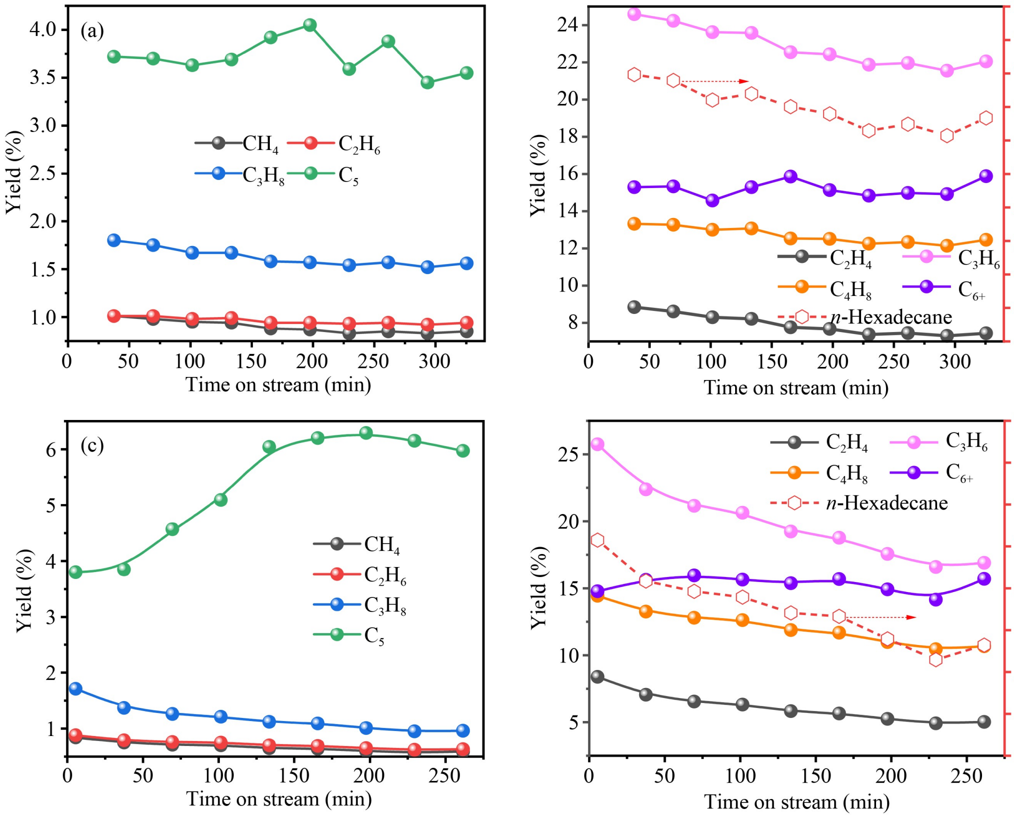

Fig. 3 The yields and conversion of various products from the cracking of *n*-hexadecane catalyzed by (a, b) ZSM-5 (50) molecular sieves and (c, d) ZSM-5 (131) molecular sieves. Reaction conditions: T = 600 °C, atmospheric pressure, alkane WHSV = 10 g·g^{-1}·h^{-1}, carrier gas (N$_2$) flow rate of 100 mL·min^{-1}, TOS = 5.5 min.

3.5 Cracking of *n*-alkanes with different carbon chain over microsphere catalyst

To investigate the cracking behavior of *n*-alkanes with different carbon numbers over microsphere catalysts, *n*-octane and *n*-hexadecane were selected as model reactants to examine the cracking performance of differently sized *n*-alkanes over Cat.2$^{\#}$. Figure 4 shows the product yields and alkane conversion over Cat.2$^{\#}$. As shown in Figs. 4(a) and 4(b), with prolonged reaction time, the yields of C$_1$–C$_5$ hydrocarbons gradually decreased, while those of C$_{6+}$ hydrocarbons increased, and the conversion rate of *n*-octane progressively declined. From Figs. 4(c) and 4(d), the initial conversion of *n*-hexadecane was 53%, which rapidly dropped to approximately 2% (attributed to thermal cracking), and similar trends were observed for all product yields. Based on these results, we infer that the molecular size of the model compounds significantly impacts catalytic performance. Specifically, long-chain *n*-alkanes larger than the pore size of microsphere catalyst cannot enter the pores and rely solely on external acidic sites for cracking. In contrast, short-chain normal alkanes that are smaller or comparable in size to the catalyst pore diameter can undergo cracking either via the external acidic sites, they can also enter the catalyst pores and be cracked by the acidic sites within the pores.

Nitrogen physical adsorption-desorption characterization was performed on fresh catalyst and the catalysts after reaction with model compounds and the results are shown in Table S3 (cf. ESM). Compared to the fresh catalyst, the *n*-octane-reacted catalyst exhibited varying degrees of reduction in specific surface area, micropore surface area, total pore volume, and micropore volume. However, the reduction in the pore structure of the catalyst after the reaction with *n*-hexadecane was less significant than that after the reaction with *n*-octane. These results indicate that *n*-octane and its cracking products can readily access the pore system of Cat.2$^{\#}$, whereas *n*-hexadecane molecules, experience restricted diffusion, allowing only a small fraction of their cracked derivatives to enter the Cat.2$^{\#}$. The confinement effect and deep reactions within the pores likely promoted carbon deposition, which occupied the pore channels. These characterization results further confirm that *n*-hexadecane, due to its larger molecular dimensions, cannot diffuse into the catalyst pores. Instead, it underwent initial cracking via acid sites on the external surface. The primary products subsequently underwent cyclization and condensation reactions, rapidly forming carbon deposits that either covered the external acid sites or blocked pore entrances (Fig. S6 (cf. ESM) carbon deposition results obtained by TGA). NH$_3$-TPD results (Fig. S7 (cf. ESM)) revealed a gradual decrease in acid

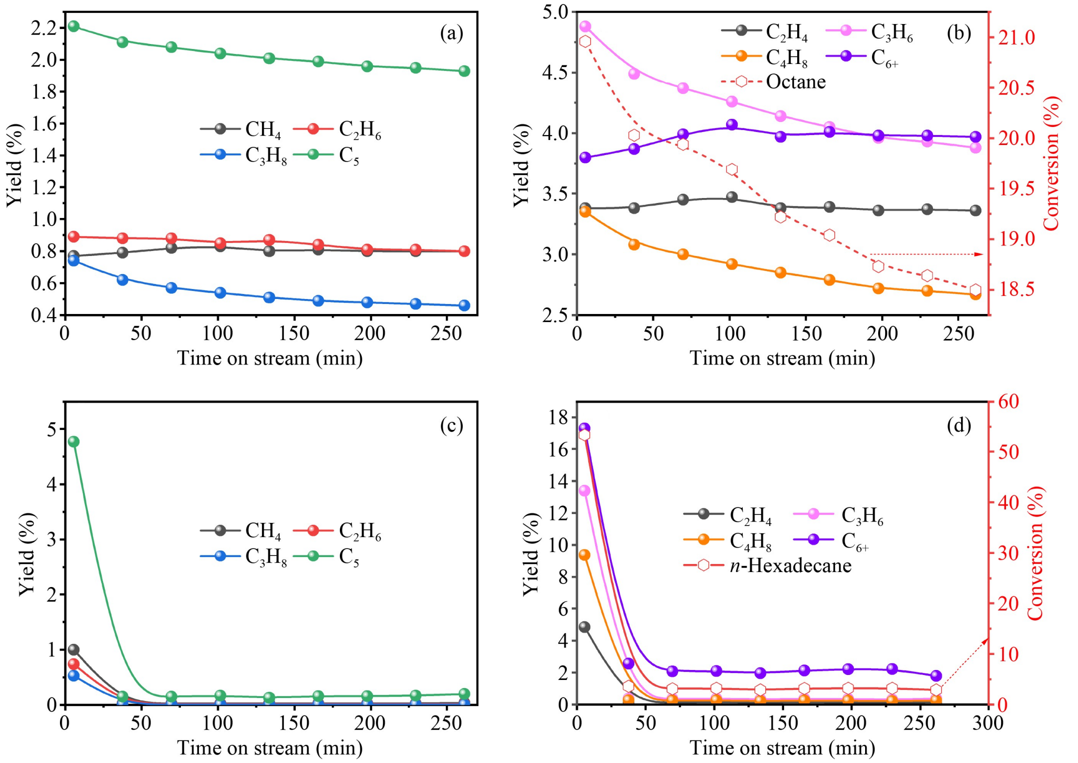

Fig. 4 Conversion and product yields of catalytic cracking of (a, b) *n*-octane and (c, d) *n*-hexadecane on Cat.$2^{\#}$. Reaction conditions: $T = 600$ °C, atmospheric pressure, alkane WHSV = 5 $g \cdot g^{-1} \cdot h^{-1}$, carrier gas ($N_2$) flow rate of 100 $mL \cdot min^{-1}$.

site concentration after reaction, attributed to acid site coverage by carbon deposits. Consequently, *n*-hexadecane failed to utilize the remaining acid sites for primary cracking, leading to rapid catalyst deactivation.

Similarly, the aforementioned cracking reaction was also conducted on Cat.$1^{\#}$ (which exhibits stronger external surface acidity than Cat.$2^{\#}$) to further deepen the understanding of the reaction mechanism. As shown in Figs. 5(a) and 5(b), within the entire reaction interval, there is no significant fluctuation in the conversion of *n*-octane and the yields of various products as reaction time increases. Figures 5(c) and 5(d) reveal that, as the reaction time increases, *n*-hexadecane on the Cat.$1^{\#}$ can still maintain a conversion of approximately 85% at 260 min. Additionally, the entire reaction process remains largely stable, with the yields of various products remaining almost unchanged. Table S4 (cf. ESM) summarizes the pore structure parameters of fresh and used catalysts after *n*-octane and *n*-hexadecane reactions. Compared to fresh catalysts, the used catalysts exhibited reduced specific surface area, micropore surface area, external surface area (excluding micropores), pore volume, and micropore volume. This phenomenon can be attributed to the strong external acidity of Cat.$1^{\#}$, where alkane molecules continuously interact with acid sites on the catalyst surface, undergoing cracking. The resulting smaller cracked products, with dimensions below the pore size of microsphere catalyst, diffuse into the catalyst channels. The confined pore space and diffusion limitations promote deep reactions such as condensation and cyclization, leading to significant carbon deposition and partial pore blockage. Furthermore, as the carbon number of the alkanes increases, the pore blockage becomes more severe.

Through in situ FTIR spectroscopy analysis, the dynamic evolution of key intermediate products during the conversion of *n*-octane over microsphere catalysts was clearly observed (Fig. 6). As shown in Figs. 6(b) and 6(d), the characteristic peaks located at 1579/1583, 1434/1456, and 1349/1386 cm^{-1} are assigned to the C=C stretching vibration of the aromatic ring skeleton, the antisymmetric bending vibration of methylene groups, and the symmetric scissoring bending vibration of methyl groups, respectively [44]. This indicates the formation of alkyl-substituted aromatic hydrocarbon intermediates during the reaction. Furthermore, the intensity of these intermediate peaks continuously increased over time, signifying their continuous generation and accumulation on the catalyst surface or within the system. As shown in Figs. 6(a) and 6(c), the characteristic peaks at 2966/2967, 2931/2933, and 2871/2875 cm^{-1} are assigned to the C–H vibrational peaks of physically adsorbed *n*-octane [45,46]. The peaks at 3062 and 3066 cm^{-1} are assigned to the C–H stretching vibrations on aromatic rings [44]. Critically, the vibrational intensity was significantly higher for microsphere Cat.$1^{\#}$ compared to Cat.$2^{\#}$. This demonstrates that microsphere catalysts with stronger external surface acidity are more prone to the formation

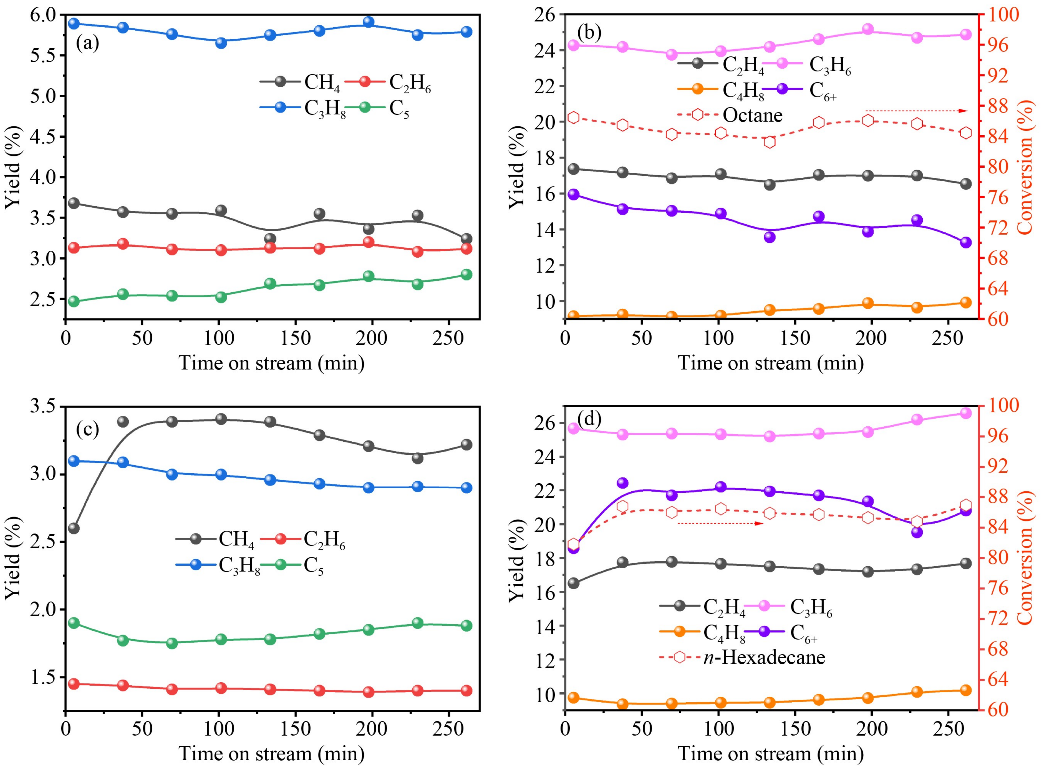

Fig. 5 The conversions and yields of various products from the cracking of (a, b) *n*-octane and (c, d) *n*-hexadecane catalyzed by Cat.1[#]. Reaction conditions: T = 600 °C, atmospheric pressure, alkane WHSV = 5 $g \cdot g^{-1} \cdot h^{-1}$, carrier gas ($N_2$) flow rate of 100 $mL \cdot min^{-1}$.

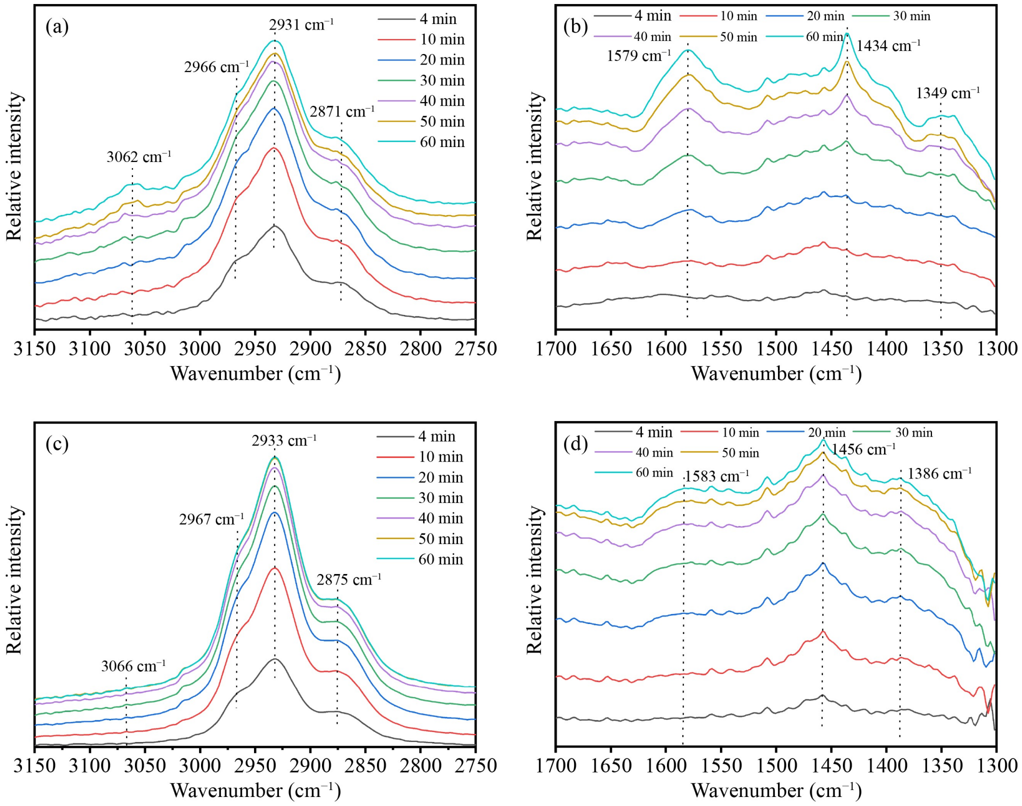

Fig. 6 FTIR difference spectra of *n*-octane conversion catalyzed by microsphere (a, b) Cat.1[#] and (c, d) Cat.2[#] at 600 °C.

of polycyclic aromatic hydrocarbons.

High-resolution Fourier transform ion cyclotron resonance mass spectrometry (FT-ICR-MS) analysis of heavy coke components deposited on microspherical catalysts and ZSM-5 zeolite following *n*-hexadecane reaction revealed detectable coke species within a mass range of 200–1200 Da. As illustrated in the corresponding Fig. 7, the microspherical catalysts exhibited a greater propensity to form higher-carbon-number unsaturated hydrocarbons compared to the ZSM-5 zeolite. Furthermore, the strength of surface acidity on the microspherical catalysts demonstrated a positive correlation with the carbon number of the generated coke species. This observed trend aligns with results obtained from *in situ* FTIR characterization monitoring the conversion of alkanes over the microspherical catalysts. Thus, it is inferred that the microsphere catalyst with strong external surface acidity deactivates slowly but generates more polycyclic aromatic hydrocarbons, because the acidic sites on the external surface of the microspheres dominate the entire reaction chain from long-chain alkanes to PAHs, and the sites themselves have certain tolerance to deep carbon deposition or can promote the conversion of partial intermediates. In contrast, the microsphere catalyst with weak external surface acidity deactivates rapidly but produces less PAHs, which is attributed to the fact that its weak acidic sites are difficult to drive deep aromatization and are extremely easily covered by heavy intermediates generated in the initial stage of the reaction, leading to the rapid loss of active sites and hindering subsequent reactions.

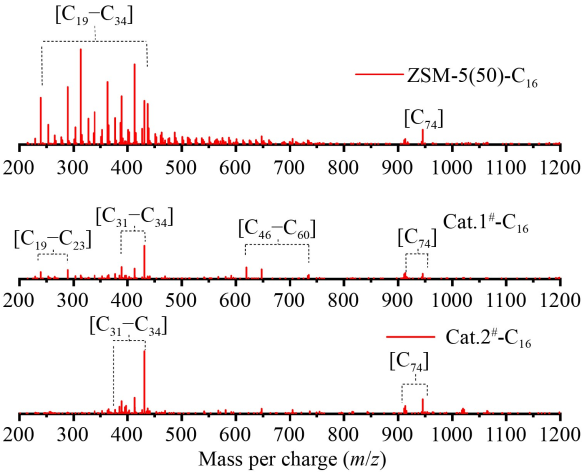

Fig. 7 FT-ICR-MS results. Reaction conditions: T = 600 °C, WHSV of *n*-hexadecane = 5 $g \cdot g^{-1} \cdot h^{-1}$, atmospheric pressure. The microspherical catalysts and zeolite were removed after 2 h of reaction.

Based on the experimental observations and discussion, we propose a rational mechanistic model for the cracking of different chain-length *n*-alkanes on catalyst microspheres, as illustrated in Fig. 8. The model demonstrates distinct reaction pathways governed by molecular dimensions: the conversion of long-chain *n*-alkanes over microsphere catalysts proceeds through two consecutive stages: initially, the reactant molecules undergo primary cracking at the surface acidic sites of the microspheres, generating intermediate products with reduced molecular weight. Subsequently, these secondary products diffuse into the internal pore channels through molecular diffusion, where they undergo further deep cracking reactions at the acidic active sites within the nanoconfined environments. This spatially differentiated reaction pathway ultimately achieves efficient conversion of large alkane molecules through hierarchical catalytic processes [47–50].

4 Conclusions

The cracking behavior of co-feeding methanol and *n*-alkanes with different carbon numbers over microsphere catalysts was investigated, along with the cracking characteristics of *n*-alkanes with varying kinetic diameters on microsphere catalysts and ZSM-5 zeolites. The key conclusions are summarized as follows.

In the co-feeding system of methanol and *n*-alkanes, the conversion and olefins yield increased with the increasing of alkane carbon numbers. The weaker external surface

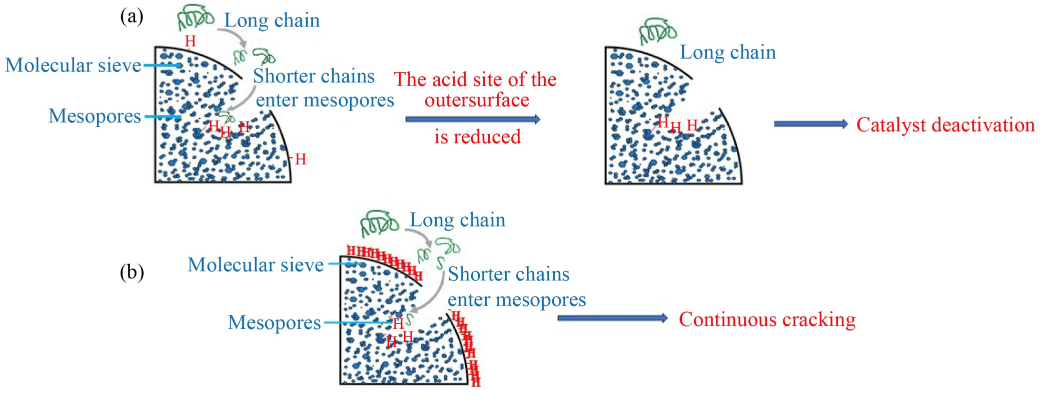

Fig. 8 The cracking mechanism of long-chain *n*-alkanes over microspherical catalysts.

acidity of microsphere catalyst reduces the relative proportion of by-products (C_1–C_4 alkanes) while enhancing the yield of C_2–C_4 olefins, effectively suppressing secondary reactions such as olefin aromatization and hydrogen transfer reaction. Conversely, stronger external surface acidity significantly promotes secondary reactions (for example, isomerization, hydrogen transfer, and cyclization), leading to increasing yields of BTX aromatics at the expense of olefin production.

The kinetic diameter of *n*-hexadecane exceeds the pore size of the active ZSM-5 zeolite component in the microspherical catalyst, preventing its entry into the internal pores. Consequently, its cracking predominantly occurs on the external surface of the catalyst. The resulting cracked products may subsequently diffuse into the pore channels, where they could undergo further reactions at internal acid sites. In contrast, *n*-octane exhibits a kinetic diameter comparable to or slightly larger than the pore size of ZSM-5 zeolite. This enables a dual cracking mechanism: a portion of *n*-octane molecules undergo surface-initiated cracking on the external catalyst surface, while others penetrate the pore channels to access internal acid sites. Both external and internal acid sites thereby synergistically contribute to the cracking process of *n*-octane. Therefore, in the industrial catalytic treatment of heavier naphtha fractions, it is recommended to enhance the external surface acidity of catalyst microspheres. By implementing a hierarchical catalysis mechanism, stepwise conversion of the feedstock can be achieved, thereby improving the selectivity of target products. Additionally, appropriate enlargement of pore size can enhance the mass transfer rate of macromolecular substances, reducing carbon deposition caused by their retention in the pore channels and thus prolonging the service life of the catalyst.

Distinct differences exist between ZSM-5 zeolites and microsphere catalysts in catalyzing long-chain *n*-alkanes (*n*-C_{16}). For catalysts, binders, and other substances are added to the molecular sieve powder during the manufacturing process, which changes the original active sites and pore size of the molecular sieve, so the outer surface acidity and pore size are particularly important in catalyzing alkanes with different chain lengths. In contrast, pure ZSM-5 zeolites allow long-chain alkanes ($> C_{10}$) to adjust their molecular configurations at elevated temperatures, facilitating entry into the zeolite pores for internal cracking.

Competing interests The authors declare that they have no competing interests.

Acknowledgements This research was funded by the National Natural Science Foundation of China (Grant Nos. 21991093 and 21991090).

Electronic Supplementary Material Supplementary material is available in the online version of this article at https://doi.org/10.1007/s11705-026-2635-9 and is accessible for authorized users.

References

1. Alotaibi F M, González-Cortés S, Alotibi M F, Xiao T, Al-Megren H, Yang G, Edwards P P. Enhancing the production of light olefins from heavy crude oils: turning challenges into opportunities. Catalysis Today, 2018, 317: 86–98
2. Yan H F. Process progress in catalytic cracking for more low-carbon olefins. Modern Chemical Industry, 2020, 40(12): 73–76
3. Hou K J, Gao J S, Ma A, Wang G, Wang Z F, Gao Y F, Liu C W. Research progress in heavy oil catalytic pyrolysis technology for light olefins. Chinese Journal of Applied Chemistry, 2022, 51(11): 3278–3284 (in Chinese)
4. Ning M, Fan F, Lu P, Bai F, Hua C, Liu H. Technology for utilization of naphtha resources as by-product of heavy oil catalytic cracking. Natural Gas Chemical Industry, 2019, 44(6): 93–97 (in Chinese)
5. Zhu J, Cui Y, Chen Y, Zhou H, Wang Y, Wei F. Recent researches on process from methanol to olefins. Journal of Chemical Industry and Engineering, 2010, 61(7): 1674–1684 (in Chinese)
6. Ghaedi M, Izadbakhsh A. Effects of Ca content on the activity of HZSM-5 nanoparticles in the conversion of methanol to olefins and coke formation. Journal of Fuel Chemistry & Technology, 2021, 49(10): 1468–1486
7. Khezri H, Izadbakhsh A, Izadpanah A A. Promotion of the performance of La, Ce, and Ca impregnated HZSM-5 nanoparticles in the MTO reaction. Fuel Processing Technology, 2020, 199: 106253
8. Hajimirzaee S, Soleimani Mehr A, Ghavipour M, Vatankhah M, Behbahani R M. Effect of metal loading on catalytic activity and selectivity of ZSM-5 zeolite catalyst in conversion of methanol to olefins and aromatics. Petroleum Science and Technology, 2017, 35(3): 279–286
9. Sakha M R, Halimitabrizi P, Soltanali S, Ektefa F, Hajjar Z, Salari D. Sustainable product-based approach in the production of olefins using a dual functional ZSM-5 catalyst. RSC Advances, 2023, 13(11): 7514–7523
10. Xia W, Wang J, Wang L, Qian C, Ma C, Huang Y, Fan Y, Hou M, Chen K. Ethylene and propylene production from ethanol over Sr/ZSM-5 catalysts: a combined experimental and computational study. Applied Catalysis B: Environmental, 2021, 294: 120242
11. Ye M, Tian P, Liu Z. DMTO: a sustainable methanol-to-olefins technology. Engineering, 2021, 7(1): 17–21
12. Yang M, Fan D, Wei Y X, Tian P, Liu Z M. Recent Progress in methanol-to-olefins (MTO) catalysts. Advanced Materials, 2019, 31(50): 1902181
13. Tian P, Wei Y, Ye M, Liu Z. Methanol to olefins (MTO): from fundamentals to commercialization. ACS Catalysis, 2015, 5(3): 1922–1938
14. Olah G A. Beyond oil and gas: the methanol economy. Angewandte Chemie International Edition, 2005, 44(18): 2636–2639
15. Cai R, Zhu H X, Li W J, Xiao Y, Liu Z M. Development path of energy science and technology under dual carbon goals: perspective of multi-energy system integration. Bulletin of the

Chinese Academy of Sciences, 2022, 37(4): 502–510 (in Chinese)

16. Shih C F, Zhang T, Li J, Bai C. Powering the future with liquid sunshine. Joule, 2018, 2(10): 1925–1949
17. Olah G A. Towards oil independence through renewable methanol chemistry. Angewandte Chemie International Edition, 2013, 52(1): 104–107
18. Vogt E T C, Weckhuysen B M. Fluid catalytic cracking: recent developments on the grand old lady of zeolite catalysis. Chemical Society Reviews, 2015, 44(20): 7342–7370
19. Song Z, Takahashi A, Nakamura I, Fujitani T. Phosphorus-modified ZSM-5 for conversion of ethanol to propylene. Applied Catalysis A: General, 2010, 384(1): 201–205
20. Lv J, Hua Z, Ge T, Zhou J, Zhou J, Liu Z, Guo H, Shi J. Phosphorus modified hierarchically structured ZSM-5 zeolites for enhanced hydrothermal stability and intensified propylene production from 1-butene cracking. Microporous and Mesoporous Materials, 2017, 247: 31–37
21. Kong D J, Zou W, Tong W Y, Fang D Y. Synthesis and catalytic behaviors of MFI/MFI core-shell zeolite. Acta Chimica Sinica, 2009, 67(15): 1765–1770 (in Chinese)
22. Kong D J, Liu Z C, Fang D Y. Epitaxial growth of core-shell ZSM-5/silicalite-1 with shape selectivity. Chinese Journal of Catalysis, 2009, 30(9): 885–890 (in Chinese)
23. Jung J S, Kim T J, Seo G. Catalytic cracking of *n*-octane over zeolites with different pore structures and acidities. Korean Journal of Chemical Engineering, 2004, 21(4): 777–781
24. Akhmedov V M, Al-Khowaiter S H, Al-Refai J K. Hydroconversion of C_5–C_8 alkanes over Zr-containing supported catalysts prepared by metal vapor method. Applied Catalysis A: General, 2003, 252(2): 353–361
25. Góra-Marek K, Tarach K, Choi M. 2,6-di-*tert*-butylpyridine sorption approach to quantify the external acidity in hierarchical zeolites. Journal of Physical Chemistry C, 2014, 118(23): 12266–12274
26. Pham T N, Nguyen V, Nguyen-Phu H, Wang B, Crossley S. Influence of Brønsted acid site proximity on alkane cracking in MFI zeolites. ACS Catalysis, 2023, 13(2): 1359–1370
27. Janda A, Vlaisavljevich B, Lin L C, Mallikarjun Sharada S, Smit B, Head-Gordon M, Bell A T. Adsorption thermodynamics and intrinsic activation parameters for monomolecular cracking of *n*-alkanes on Brønsted acid sites in zeolites. Journal of Physical Chemistry C, 2015, 119(19): 10427–10438
28. Sánchez P, Dorado F, Ramos M J, Romero R, Jiménez V, Valverde J L. Hydroisomerization of C_6–C_8 *n*-alkanes, cyclohexane and benzene over palladium and platinum beta catalysts agglomerated with bentonite. Applied Catalysis A: General, 2006, 314(2): 248–255
29. Corma A, Marie O, Ortega F J. Interaction of water with the surface of a zeolite catalyst during catalytic cracking: a spectroscopy and kinetic study. Journal of Catalysis, 2004, 222(2): 338–347
30. Peng P, Gao X H, Yan Z F, Mintova S. Diffusion and catalyst efficiency in hierarchical zeolite catalysts. National Science Review, 2020, 7(11): 1726–1742
31. Du Y Z, Qin B, Wang H G, Hao W Y, Gao H, Fang X C. Development of hierarchical zeolites in hydrocracking catalysts of heavy oil. Chemical Industry and Engineering Progress, 2021, 40(4): 1859–1867
32. Xu H, Lei C, Wu Q, Zhu Q, Meng X, Dai D, Maurer S, Parvulescu A N, Müller U, Xiao F. Organosilane surfactant-assisted synthesis of mesoporous SSZ-39 zeolite with enhanced catalytic performance in the methanol-to-olefins reaction. Frontiers of Chemical Science and Engineering, 2020, 14(2): 267–274
33. Kokotailo G T, Lawton S L, Olson D H, Meier W M. Structure of synthetic zeolite ZSM-5. Nature, 1978, 272(5652): 437–438
34. Wu J. Research on the correlation between dynamic diameters of hydrocarbon molecules and zeolites shape-selective catalytic performance. Chemical Industry and Engineering Progress, 2016, 35(1): 167–173 (in Chinese)
35. Urata K, Furukawa S, Komatsu T. Location of coke on H-ZSM-5 zeolite formed in the cracking of *n*-hexane. Applied Catalysis A: General, 2014, 475: 335–340
36. Vogt E T C, Fu D L, Weckhuysen B M. Carbon deposit analysis in catalyst deactivation, regeneration, and rejuvenation. Angewandte Chemie International Edition, 2023, 62(29): e202300319
37. Mores D, Kornatowski J, Olsbye U, Weckhuysen B M. Coke formation during the methanol-to-olefin conversion: *in situ* microspectroscopy on individual H-ZSM-5 crystals with different Brønsted acidity. Chemistry, 2011, 17(10): 2874–2884
38. Wang N, Sun W, Hou Y, Ge B, Hu L, Nie J, Qian W, Wei F. Crystal-plane effects of MFI zeolite in catalytic conversion of methanol to hydrocarbons. Journal of Catalysis, 2018, 360: 89–96
39. Fu D, van der Heijden O, Stanciakova K, Schmidt J E, Weckhuysen B M. Disentangling reaction processes of zeolites within single-oriented channels. Angewandte Chemie International Edition, 2020, 59(36): 15502–15506
40. Müller S, Liu Y, Vishnuvarthan M, Sun X, van Veen A C, Haller G L, Sanchez-Sanchez M, Lercher J A. Coke formation and deactivation pathways on H-ZSM-5 in the conversion of methanol to olefins. Journal of Catalysis, 2015, 325: 48–59
41. Lee S, Choi M. Unveiling coke formation mechanism in MFI zeolites during methanol-to-hydrocarbons conversion. Journal of Catalysis, 2019, 375: 183–192
42. Mores D, Stavitski E, Kox M H F, Kornatowski J, Olsbye U, Weckhuysen B M. Space- and time-resolved *in situ* spectroscopy on the coke formation in molecular sieves: methanol-to-olefin conversion over H-ZSM-5 and H-SAPO-34. Chemistry, 2008, 14(36): 11320–11327
43. Zhang X, Cheng D G, Chen F, Zhan X. The role of external acidity of hierarchical ZSM-5 zeolites in *n*-heptane catalytic cracking. ChemCatChem, 2018, 10(12): 2655–2663
44. Gao F, Jia Z, Cui Z, Li Y D, Jiang H. Evolution of macromolecular structure during coal oxidation *via* FTIR, XRD and Raman. Fuel Processing Technology, 2024, 262: 108114
45. Zhu N, Wang Y, Cheng D G, Chen F Q, Zhan X L. Experimental evidence for the enhanced cracking activity of *n*-heptane over steamed ZSM-5/mordenite composite zeolites. Applied Catalysis A: General, 2009, 362(1): 26–33
46. Kotrel S, Rosynek M P, Lunsford J H. Origin of first-order kinetics during the bimolecular cracking of *n*-hexane over

H-ZSM-5 and H-β zeolites. Journal of Catalysis, 2000, 191(1): 55–61

47. Rejman S, Vollmer I, Werny M J, Vogt E T C, Meirer F, Weckhuysen B M. Transport limitations in polyolefin cracking at the single catalyst particle level. Chemical Science, 2023, 14(37): 10068–10080
48. Rejman S, Reverdy Z M, Bör Z, Louwen J N, Rieg C, Dorresteijn J M, van der Waal J K, Vogt E T C, Vollmer I, Weckhuysen B M. External acidity as performance descriptor in polyolefin cracking using zeolite-based materials. Nature Communications, 2025, 16(1): 2980
49. Serrano D P, Aguado J, Escola J M, Rodríguez J M. Influence of nanocrystalline HZSM-5 external surface on the catalytic cracking of polyolefins. Journal of Analytical and Applied Pyrolysis, 2005, 74(1): 353–360
50. Karreman M A, Buurmans I L C, Geus J W, Agronskaia A V, Ruiz-Martínez J, Gerritsen H C, Weckhuysen B M. Integrated laser and electron microscopy correlates structure of fluid catalytic cracking particles to Brønsted acidity. Angewandte Chemie International Edition, 2012, 51(6): 1428–1431